

Image Reconstruction in Phase-Contrast CT with Shortened Scans

Zheng Zhang^a, Buxin Chen^a, Dan Xia^a, Emil Y. Sidky^a, Mark Anastasio^c, and Xiaochuan Pan^{a,b}

^aDepartment of Radiology, The University of Chicago, Chicago, IL, USA

^bDepartment of Radiation & Cellular Oncology, The University of Chicago, Chicago, IL, USA

^cDepartment of Bioengineering, The University of Illinois at Urbana-Champaign, Champaign, IL, USA

ABSTRACT

Phase-contrast CT (PCCT) is an emerging tool that has found numerous applications, including applications to preclinical imaging. There remains a need for reducing the imaging time in current PCCT. One approach to reducing imaging time is to reduce the scanning angular range in PCCT. However, accurate image reconstruction from data collected over a limited angular range (LAR) is challenging because it poses a problem of accurate inversion of the PCCT imaging model that can be highly ill-conditioned in LAR scans. In this work, we conduct an investigation of accurate image reconstruction through inverting the imaging model for LAR scanning configurations in propagation-based (PB) PCCT. We have developed a directional-total-variation (DTV) algorithm for image reconstruction from knowledge of the discrete X-ray transform (DXT) over a LAR for CT imaging. Observing the mathematical similarity between the DXT in CT and the imaging model in PB-PCCT, we develop and tailor the DTV algorithm for image reconstruction from LAR data in PB-PCCT. Results of our study show that the tailored DTV algorithm can yield image reconstruction with reduced LAR artifacts that can be observed otherwise in images reconstructed by use of the existing algorithm in PB-PCCT imaging. For a given LAR, it can be divided into sub arcs of LARs. We also investigate a scanning configuration with two orthogonal arcs of LARs separated by 90° , and observe that the two-orthogonal-arc scanning configuration may allow image reconstruction more accurately than does a single-arc scanning configuration even though the total angular ranges in both scanning configurations are identical. While boundary images can be reconstructed from data, we develop the DTV algorithm for reconstruction of the image, i.e., the refractive index distribution, instead of its boundary image from data in PB-PCCT. Once the image is obtained, the Laplacian operator can be applied to it for yielding its boundary image.

Keywords: limited-angular range (LAR), directional total variation, primal-dual algorithm, phase contrast CT (PCCT)

1. INTRODUCTION

Physical quantities such as the refractive index within an object scanned can be estimated in phase-contrast CT (PCCT) for yielding unique contrast mechanisms differing from that in conventional CT. It is believed that PCCT may hold potential value for certain preclinical and clinical applications. However, a number of issues need to be addressed adequately before its wide adoption in preclinical and clinical applications. One of the practical constraints that PCCT faces is its considerably long imaging time. There exist studies on the minimization of the total imaging time by reducing the number of scanning views while maintaining the imaging time unchanged at each view in PCCT.¹⁻³ In this study, we investigate a different approach to reducing the imaging time in PCCT by lowering its scanning angular range to a limited angular range (LAR) that is less than the full angular range of π . A PCCT scan over a LAR can readily be implemented in PCCT without invoking any hardware changes simply by stopping X-ray illumination and data collection beyond the LAR prescribed. However, accurate image reconstruction from such LAR data is challenging because it poses a problem of accurate inversion of the PCCT imaging model that can be highly ill-conditioned under LAR conditions.

In this work, we conduct an investigation of accurate image reconstruction from LAR data by inverting the imaging model in propagation-based (PB) PCCT. We have developed a directional-total-variation (DTV)

algorithm⁴ for image reconstruction from knowledge of the discrete X-ray transform (DXT) over a LAR for CT imaging. Observing the mathematical similarity between the DXT in CT and the imaging model in PB-PCCT, we develop and tailor the DTV algorithm for image reconstruction from LAR data in PB-PCCT. For a given LAR, it can be divided into sub arcs of LARs. We thus also investigate a scanning configuration with two orthogonal arcs of LARs,⁵⁻⁷ which are of equal angular ranges but their centers are separated by 90°. For simplicity, we refer to a configuration with two orthogonal arcs of LARs as the two-orthogonal-arc configuration, whereas the configuration with a single arc of LAR as a single-arc configuration.

In many of the existing works in PB-PCCT, algorithms have been developed only for reconstruction of the image boundaries, as shown in Fig. 1b, instead of the image itself in Fig. 1a. Unlike these existing algorithms, the DTV algorithm developed in this work reconstructs the image, i.e., the refractive index distribution, from LAR data in PB-PCCT. From the reconstructed image, one can then readily obtain the boundary image.

2. MATERIALS AND METHODS

2.1 Imaging model in PB-PCCT

In PB-PCCT, assuming the object's attenuation of X-ray is weak, the 2D imaging model can be expressed as^{1,8}

$$\mathbf{g} = \mathcal{H}\Delta\mathbf{f}, \quad (1)$$

where vector \mathbf{g} of size M denotes model data in PB-PCCT; vector \mathbf{f} of size N denotes a 2D discrete image of the refractive index within the imaged object; $\Delta = \frac{\partial^2}{\partial x^2} + \frac{\partial^2}{\partial y^2}$ is the discrete Laplacian operator on the image space; and system matrix \mathcal{H} of size $M \times N$ represents a discrete Radon transform from image space to data space. In this work, element h_{ij} of \mathcal{H} denotes the intersection between ray j and pixel i . For given \mathcal{H} corresponding to a LAR scanning configuration discussed below, we use Eq. (1) to generate model data \mathbf{g} from numerical, realistic plant-seed phantom \mathbf{f} on a grid of 190×200 square pixels of size 0.12 mm in Fig. 1a.⁹

2.2 Scan configuration

We consider a single-arc and a two-orthogonal-arc scanning configurations,⁷ as shown in Figs. 1c and 1d, with a parallel-beam projection geometry, and the discrete Radon transform is used as the imaging model in PB-PCCT. We also assume that the former covers LAR of α_τ and that the latter includes two sub-arcs of LARs of α_1 and α_2 , symmetric relative, respectively, to the y - and x -axis. In the work, without loss of generality, we consider the case with $\alpha_\tau = \alpha_1 + \alpha_2$ and $\alpha_1 = \alpha_2$. Furthermore, the detector array consists of 512 bins of size 0.046 mm. We generate noiseless data from the plant-seed phantom (i) with the single-arc configurations of $\alpha_\tau = 60^\circ, 90^\circ, 120^\circ$, and 150° , with an angular interval of 0.5° per view, and (ii) with the two-orthogonal-arc configurations of $2\alpha_1 = 2\alpha_2 = 60^\circ, 90^\circ, 120^\circ$, and 150° . Based upon the noiseless data, we also generate noisy data which is equivalent to adding Gaussian noise to the intensity data,⁸ and the Gaussian noise has zero mean and standard deviation of 1.5% of the intensity for each detector bin.

2.3 Directional-TV reconstruction algorithm

Image reconstruction in PB-PCCT is equivalent to inverting the imaging model in Eq. (1). It is well-known that, while existing analytic algorithms can accurately reconstruct boundary images from data collected over FAR of 180° , they cannot yield accurate boundary images nor images from data collected over LARs that are considerably lower than 180° . Instead, we formulate the reconstruction problem from LAR data in PB-PCCT as an optimization problem and tailor the DTV algorithm to obtain images through solving the optimization problem.

We consider a convex optimization program containing a data- ℓ_2 -norm fidelity and DTV constraints along the x - and y -directions, which is given by⁴

$$\mathbf{f}^* = \underset{\mathbf{f}}{\operatorname{argmin}} \Phi(\mathcal{H}\Delta\mathbf{f} - \mathbf{g}^{[\mathcal{M}]}) \quad \text{s.t.} \quad \Psi(\mathbf{f}) \quad (2)$$

where vector $\mathbf{g}^{[\mathcal{M}]}$ of size M denotes discrete measured data; $\Phi(\mathcal{H}\Delta\mathbf{f} - \mathbf{g}^{[\mathcal{M}]})$ denotes the ℓ_2 -norm of the difference between $\mathcal{H}\Delta\mathbf{f}$ and measured data $\mathbf{g}^{[\mathcal{M}]}$; $\Psi(\mathbf{f})$ is the constraint term in the optimization program which includes

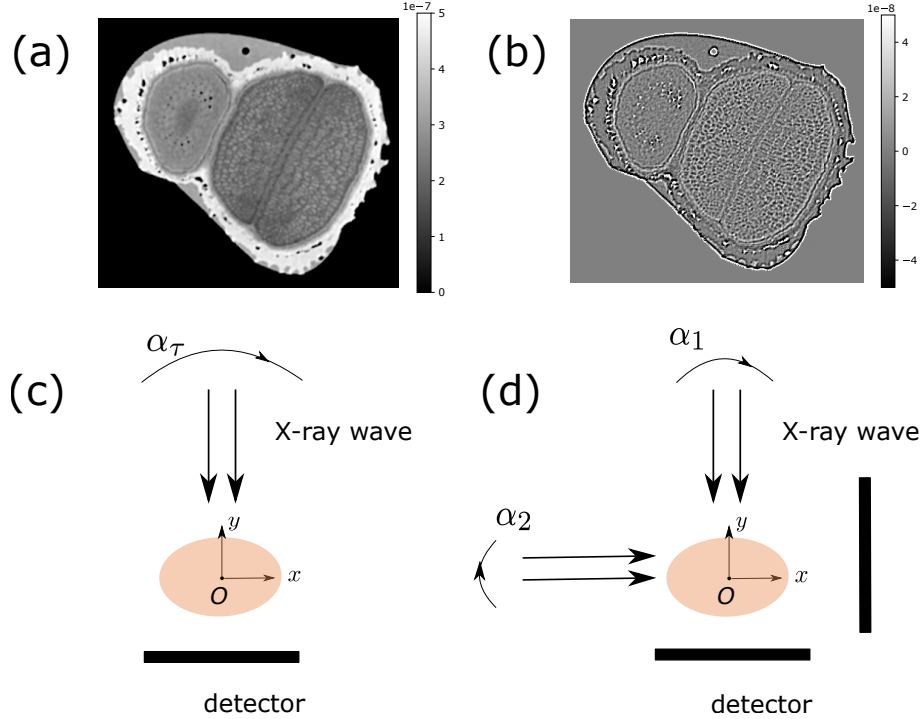


Figure 1. (a) A numerical, realistic plant-seed phantom, i.e., truth image $\mathbf{f}^{\text{[truth]}}$, from which PB-PCCT data are generated. Display window: $[0.0, 5 \times 10^{-7}]$ arbitrary units (AU); (b) a boundary image generated by applying the discrete Laplacian operator to the plant-seed phantom in panel (a). Display window: $[-5 \times 10^{-8}, 5 \times 10^{-8}]$ AU; (c) single-arc configuration with LAR of α_τ , and (d) two-orthogonal-arc configuration in which the two sub-arcs of LARs are symmetric, respectively, relative to the y - and x -axis, covering equal angular ranges α_1 and α_2 , where $\alpha_\tau = \alpha_1 + \alpha_2$.

three components: image DTV constraint along x -axis, image DTV constraint along y -axis, and image non-negativity constraint; the DTV constraint applies an upper bound on an image DTV, which is defined as ℓ_1 -norm of a vector obtained by calculating two-point differences of \mathbf{f} along either x - or y -axis; and the image non-negativity constraint is to enforce non-negative values for each pixel in the image. In many of existing works,^{1,10,11} algorithms were developed largely for inverting \mathcal{H} in the imaging model, thus yielding the boundary image $\Delta\mathbf{f}$, instead of image \mathbf{f} itself. In this work, we develop and tailor the DTV algorithm to solve Eq. (2) directly for obtaining image \mathbf{f} . Once image \mathbf{f} is obtained, one can readily apply the Laplacian to it to obtain a boundary image, as shown in Fig. 1b. For references, we also reconstruct images by using the filtered-backprojection (FBP) algorithm.^{8,12}

For evaluating image reconstructed, we first perform visual inspection of the images reconstructed. Additionally, we also perform a quantitative evaluation of image reconstructed from data over LAR by using the normalized root-mean-square-error (nRMSE) metric

$$\text{nRMSE}(\mathbf{f}^{\text{[recon]}}) = \|\mathbf{f}^{\text{[recon]}} - \mathbf{f}^{\text{[truth]}}\|_2 / \|\mathbf{f}^{\text{[truth]}}\|_2, \quad (3)$$

where $\mathbf{f}^{\text{[recon]}}$ and $\mathbf{f}^{\text{[truth]}}$ denote the reconstructed and truth images. Metric nRMSE provides measures of quantitative accuracy between the reconstructed and truth images. We note that $\text{nRMSE}(\mathbf{f}^{\text{[recon]}})$ approaches 0 as $\mathbf{f}^{\text{[recon]}}$ approaches $\mathbf{f}^{\text{[truth]}}$.

3. RESULTS

3.1 Reconstruction from noiseless data

We first conducted image reconstruction, as shown in Fig. 2, by using the DTV and FBP algorithms from noiseless data with the two-orthogonal-arc and single-arc configurations over total angular ranges $\alpha_\tau = 60^\circ, 90^\circ$,

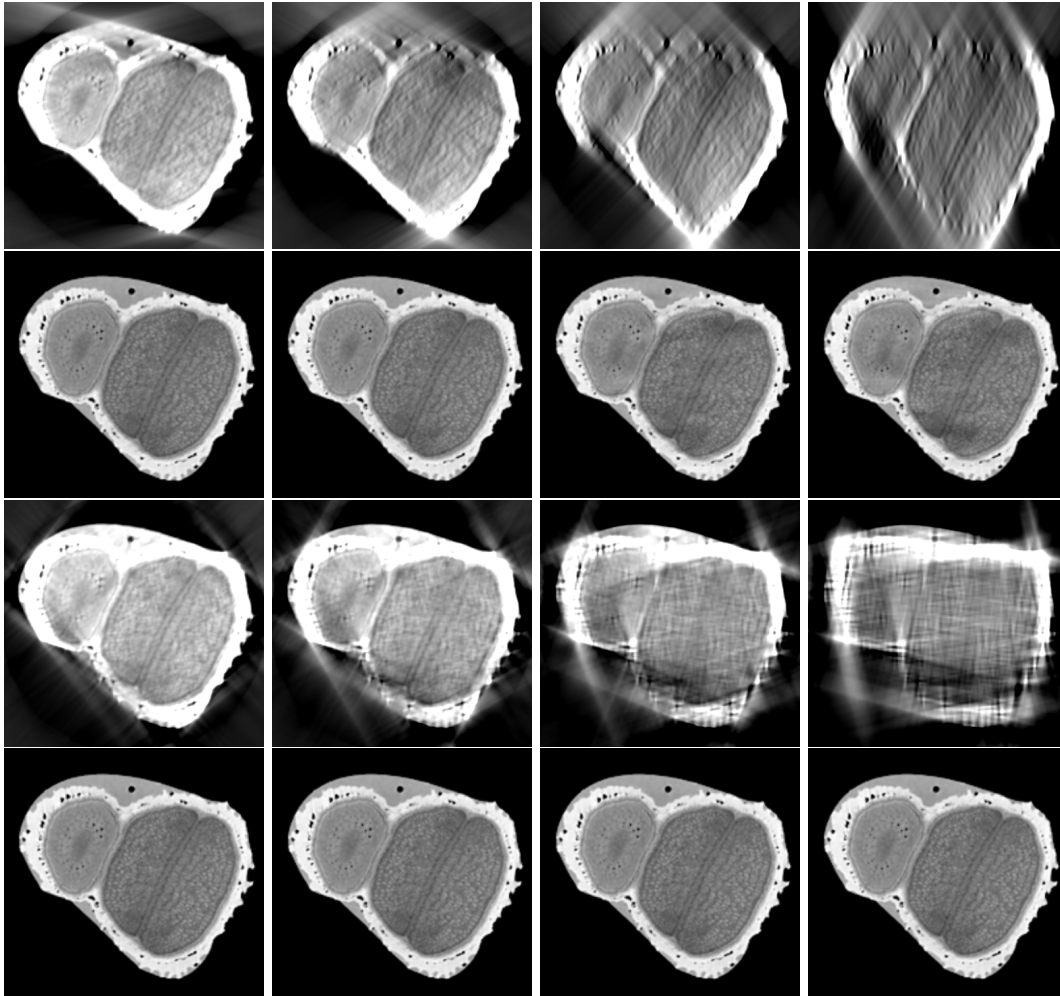


Figure 2. Images reconstructed by use of the FBP (rows 1&3) and DTV (rows 2&4) algorithm from noiseless data for single-arc configurations (rows 1&2) of $\alpha_\tau = 150^\circ$ (column 1), 120° (column 2), 90° (column 3), and 60° (column 4), respectively, and for two-orthogonal-arc configurations (rows 3&4) of $\alpha_1 = \alpha_2 = 75^\circ$ (column 1), 60° (column 2), 45° (column 3), and 30° (column 4), respectively. Display window: $[0.0, 5 \times 10^{-7}]$ AU.

Table 1. nRMSEs of images reconstructed from noiseless data generated with single-arc and two-orthogonal-arc configurations of different α_τ .

Configuration \ LAR	150°	120°	90°	60°
	Single-arc	2.56×10^{-5}	3.85×10^{-4}	1.27×10^{-2}
Two-orthogonal-arc	8.40×10^{-7}	1.63×10^{-5}	1.44×10^{-4}	2.21×10^{-3}

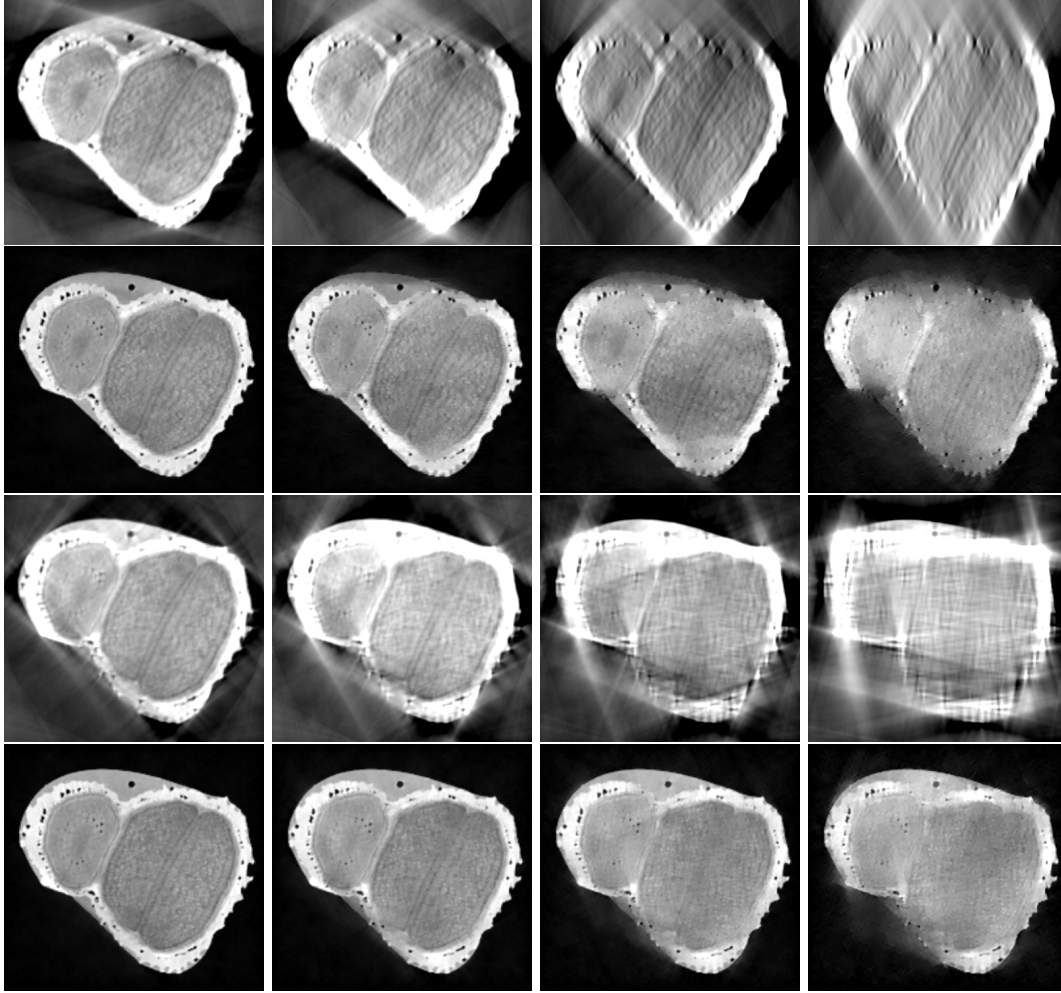


Figure 3. Images reconstructed by use of the FBP (rows 1&3) and DTV (rows 2&4) algorithm from noisy data for single-arc configurations (rows 1&2) of $\alpha_\tau = 150^\circ$ (column 1), 120° (column 2), 90° (column 3), and 60° (column 4), respectively, and for two-orthogonal-arc configurations (rows 3&4) of $\alpha_1 = \alpha_2 = 75^\circ$ (column 1), 60° (column 2), 45° (column 3), and 30° (column 4), respectively. Display window: $[0.05, 0.9]$.

120° , and 150° . In this case, measured data and model data are identical, i.e., $\mathbf{g}^{[\mathcal{M}]} = \mathbf{g} = \mathcal{H}\Delta\mathbf{f}$. We first observe that FBP reconstructions from all LAR data contain significant artifacts such as leakage and distortion. It can also be observed that all DTV reconstructions of the two-orthogonal-arc configurations visually resemble the truth plant-seed phantom. However, DTV reconstructions of the single-arc configurations show visible artifacts for $\alpha_\tau \leq 90^\circ$. We also calculated nRMSEs of the DTV reconstructions and list the corresponding values in Table 1. It can be observed that the nRMSE increases as total-angular range α_τ decreases. In addition, the nRMSEs of DTV reconstructions for two-orthogonal-arc configurations are generally smaller than those of the single-arc configurations for a given α_τ .

3.2 Reconstruction from noisy data

We then conducted image reconstruction with the DTV and FBP algorithms from noisy data $\mathbf{g}^{[\mathcal{M}]}$, as described in Sec. 2.2, by using the two-orthogonal-arc and the single-arc configurations covering total angular ranges $\alpha_\tau = 60^\circ, 90^\circ, 120^\circ$, and 150° , and show results in Fig. 3. Similarly to the noiseless-data study, there exist significant LAR artifacts in all FBP reconstructions. For the DTV reconstructions, in general, as the total angular coverage α_τ decreases, LAR artifacts increase in image reconstructions. We observe that DTV reconstructions with the two-orthogonal-arc configuration outperform those with the single-arc configuration in terms of artifacts

Table 2. nRMSEs of the DTV reconstructions from noisy data generated with single-arc and two-orthogonal-arc configurations of different α_τ .

LAR Configuration	150°	120°	90°	60°
Single-arc	0.134	0.187	0.269	0.392
Two-orthogonal-arc	0.118	0.167	0.220	0.283

reduction. This is understandable because the data model is less ill-conditioned for the former than for the latter, and thus the reconstruction of the former is less sensitive to data inconsistency, i.e., data noise, than that of the latter. In particular, DTV reconstructions with single-arc configurations considerably deteriorate for $\alpha_\tau \leq 90^\circ$, and some detailed structures cannot be identified. DTV reconstructions with two-orthogonal-arc configurations, however, can still reveal most of the structures for $\alpha_\tau = 60^\circ$. We also conduct a quantitative analysis of the DTV reconstructions by computing their nRMSEs relative to the truth phantom, and show results in Table 2. We notice that, for DTV reconstructions from LAR data containing noise, the nRMSEs of reconstructions with the two-orthogonal-arc configuration are smaller than those of reconstructions with the single-arc configuration. Additionally, the nRMSE increases as the total angular range decreases.

4. DISCUSSION

In the work, we have investigated image reconstruction from LAR data in PB-PCCT by developing and tailoring the DTV algorithm that was developed previously for image reconstruction from LAR data in CT. We note that the DTV algorithm developed reconstructs the image, i.e., the refractive index distribution, and that the application of the Laplacian operator to the image subsequently yields its boundary image. We have studied and compared images reconstruction for single-arc and two-orthogonal-arc configurations of different LARs. Results of our study show that the DTV algorithm developed can reconstruct images, instead of their boundary images, directly from data in PB-PCCT, and that the DTV images from LAR data are with reduced LAR artifacts observed otherwise in images reconstructed with other algorithms. Furthermore, observations can also be made that the two-orthogonal-arc configurations can further improve reconstruction accuracy of the single-arc configurations with $\alpha_\tau = \alpha_1 + \alpha_2$, especially as α_τ is reduced. This work may provide insights into the design of LAR scanning configurations for potentially reducing imaging time in PCCT. In the future, it is of interest to investigate image reconstructions from LAR data with additional noise and also for two-orthogonal-arc configurations with $\alpha_1 \neq \alpha_2$. Moreover, the DTV algorithm can also be applied to other PCCT imaging techniques to enabling LAR imaging, such as analyzer-crystal-based PCCT and grating-based PCCT.

ACKNOWLEDGMENTS

This work was supported in part by NIH Grant Nos. R01-EB026282, R01-EB023968, and 1R21CA263660-01A1. The contents of this article are solely the responsibility of the authors and do not necessarily represent the official views of the National Institutes of Health.

REFERENCES

- [1] Sidky, E. Y., Anastasio, M. A., and Pan, X., “Image reconstruction exploiting object sparsity in boundary-enhanced X-ray phase-contrast tomography,” *Opt. Expr.* **18**(10), 10404–10422 (2010).
- [2] Wang, L., Li, X., Wu, M., Zhang, L., and Luo, S., “A sparse-projection computed tomography reconstruction method for in vivo application of in-line phase-contrast imaging,” *Biomed. Engin. Onlin.* **12**(1), 1–13 (2013).
- [3] Gaass, T., Potdevin, G., Bech, M., Noël, P., Willner, M., Tapfer, A., Pfeiffer, F., and Haase, A., “Iterative reconstruction for few-view grating-based phase-contrast CTAn in vitro mouse model,” *Europhy. Lett.* **102**(4), 48001 (2013).
- [4] Zhang, Z., Chen, B., Xia, D., Sidky, E. Y., and Pan, X., “Directional-TV algorithm for image reconstruction from limited-angular-range data,” *Medical Image Analysis*, 102030 (2021).
- [5] Chen, B., Zhang, Z., Xia, D., Sidky, E. Y., and Pan, X., “Dual-energy CT imaging with limited-angular-range data,” *Phys. Med. Biol.* **66**(18), 185020 (2021).

- [6] Chen, B., Zhang, Z., Xia, D., Sidky, E. Y., and Pan, X., “Dual-energy CT imaging over non-overlapping, orthogonal arcs of limited-angular ranges,” *J. X-Ray Sci. and Technol.* **29**(6), 975–985 (2021).
- [7] Zhang, Z., Chen, B., Xia, D., Sidky, E. Y., and Pan, X., “Image reconstruction from data over two orthogonal arcs of limited-angular ranges,” *Med. Phys.* , –In Press (2022).
- [8] Bronnikov, A. V., “Theory of quantitative phase-contrast computed tomography,” *JOSA A* **19**(3), 472–480 (2002).
- [9] “MITOS,” (2018).
- [10] Köhler, T., Brendel, B., and Roessl, E., “Iterative reconstruction for differential phase contrast imaging using spherically symmetric basis functions,” *Med. Phy.* **38**(8), 4542–4545 (2011).
- [11] Nilchian, M., Vonesch, C., Modregger, P., Stampanoni, M., and Unser, M., “Fast iterative reconstruction of differential phase contrast X-ray tomograms,” *Opt. Expr.* **21**(5), 5511–5528 (2013).
- [12] Gureyev, T. E., Myers, G. R., Nesterets, Y. I., Paganin, D. M., Pavlov, K. M., and Wilkins, S. W., “Stability and locality of amplitude and phase contrast tomographies,” in [*Proc. SPIE Develop. in X-Ray Tomogr. V*], **6318**, 278–292, SPIE (2006).